ELSEVIER

J. Non-Newtonian Fluid Mech. 94 (2000) 159–177

Journal of Non-Newtonian Fluid Mechanics

www.elsevier.com/locate/jnnfm

The significance of slip in matching polyethylene processing data with numerical simulation

K. Lee, M.R. Mackley*

Department of Chemical Engineering, University of Cambridge, Pembroke Street, Cambridge CB2 3RA, UK

Received 2 June 2000

Abstract

Precise measurements of pressure difference (ΔP) in capillary and slit flow of a commercial grade linear low-density polyethylene (LLDPE) were carried out using a multi-pass rheometer (MPR) fitted with stainless-steel die inserts. In addition, the experimental stress field for slit flow was determined from isochromatic retardation bands of the flow-induced birefringence (FIB) patterns by assuming the linear stress optical rule to be valid. The MPR results were compared with steady-state numerical predictions of the viscoelastic integral Wagner model, simulated using a finite element code, POLYFLOW. The effect of slip boundary conditions on the numerical predictions of ΔP and slit principal stress difference (PSD) was investigated; the comparison was made for the capillary ΔP data obtained at two temperatures (170 and 190°C) and the slit results at 170°C. For the lower stress data at 190°C, a good match between experiment and simulation was obtained. At the lower temperature and higher stress it was necessary to introduce slip in order to match the results. Non-isothermal power law simulations suggest that shear heating effects cannot fully explain the low temperature extreme L/D data. Therefore, we tentatively conclude the necessity to introduce a wall high shear stress slip effect.

For the slit geometry, the centreline principal stress difference birefringence tracking shows good agreement with the simulations. It was found that the simulated centreline |PSD| was not very sensitive to the addition of wall slip. However, in order to obtain a good match with the overall pressure difference for the slit geometry, it was again necessary to introduce a slip component at the wall.

Keywords: Slip; Viscous heating; LLDPE; Multi-pass rheometer; K-B.K.Z.-Wagner; Axisymmetric; Planar; Birefringence

1. Introduction

In recent years, considerable advances have taken place in the numerical simulation of viscoelastic processing flows (see for example [1]). This enables detailed comparison to be made between numerical simulation and experimental capillary and flow-birefringence data (see for example [1–4]). In matching

* Corresponding author. Tel.: +44-1223-334-777; fax: +44-1223-334-796; http://www.cheng.cam.ac.uk/groups/polymer/RMP.
E-mail address: mrm1@cheng.cam.ac.uk (M.R. Mackley).

0377-0257/00/$ – see front matter
PII: S0377-0257(00)00147-6

experimental data to numerical predictions, there are potentially many adjustable parameters and variables. For experimental flow birefringence and pressure difference measurements, there is a requirement for precise optical resolution, flow rate, temperature and pressure monitoring (see for example [5]). In relation to the numerical simulation, the numerical techniques, simulation convergence criteria and grid layout are crucial aspects. In addition to this, there is considerable scope for the choice of the constitutive equation used and the choice of parameters used within any of these equations [6,7].

The possibility of the occurrence of slip in a polymer flow has been studied [8–11] and is particularly relevant to polymer processing events that occur near the wall [12,13]. In particular, at very high shear stresses a polymer melt flow can violate the classical no-slip hydrodynamic boundary condition at solid surfaces by exhibiting flow instabilities and complex non-linear dynamics [14,15]. A reduction in the polymer-wall interfacial adhesion can modify process efficiency, and wall slip has long been believed to contribute to the onset of certain melt flow instabilities that limit the production rate of many polymer processing operations [16–18]. During the extrusion of molten polymers at high stresses, the surface or shape of extrudate is often impaired by flow defects such as *melt flow instability*, *extrudate swelling*, *sharkskin* and *mattness* [19]. Some authors have associated the onset of these melt flow instabilities with different slip phenomena observed within the die [9,16,20].

The extrusion behaviour of very high molecular mass polymers, notably LLDPE and HDPE can be improved by the addition of processing aids such as fluorocarbon elastomers, which are strategically added to the polymer to enhance slip [21]. Similar improvements can be obtained through the modification of the die surface conditions (i.e. without adding chemical to the polymers extruded) using low energy PTFE (polytetrafluoroethylene) surface [22] and fluoropolymer or Teflon^{TM} coating to promote interfacial slip [23–26].

In general, the evidence for slip is indirect, e.g. the non-invariance of flow curves with die radius (see for example [27,28]). The concept of slip was first addressed by Mooney (1931), who found that certain flow curves (which were determined using capillaries of different radii) depended on the radius of the capillary once the shear stress exceeded a critical value [29]. The *Mooney* technique has been used in several studies to quantify the slip velocity for a variety of polyethylene melts using capillary and sliding plate rheometers or squeeze flow [30–33].

Direct visual observations of slip near or at the solid surfaces have been carried out using particle tracers to seed the fluid and viewing the motion of the particles with optical microscope or laser-differential velocimetry. A sophisticated method that uses evanescent-wave-induced fluorescence and fringe recovery after photobleaching to measure slip velocities at high resolution was developed by Migler et al. [34]. A tracer technique for studying shear and extensional flow in a mould cavity during injection moulding [35] has been applied to study slip properties of polymer melts [36]. In addition, the laser-Doppler velocimetry (LDV) has been used for the accurate determination of velocity with high temporal and spatial resolution. However, only a few LDV measurements on polymer melts are available in the literature (see for example [37]). In relation to wall slip, the LDV measurements of a HDPE flow in a planar slit geometry by Mackley and Moore (1986) indicated a finite fluid velocity at the wall [38]. Recently, Münstedt et al. studied *stick* and *slip* phenomena of a linear and a long-chain branched polyethylene melt in a slit die using LDV. They reported no wall slip for the long-chain branched PE in the range of shear rates applied, but pronounced wall slip for the linear PE at low apparent shear rates [39].

The flow birefringence technique for observing the steady-state polymer flow through capillaries or slit dies has been applied extensively (see for example [2–4]). Stress fields have also been characterised for unsteady flows by observation of birefringence patterns (and isochromatics) before and after onset of a critical instability [9,40]. The results for a silicone gum indicated that wall slippage occurred above a

critical stress and the fluctuation of birefringence was in phase with the extrudate distortion [9]. It has been reported that continuous slippage of a polymer and gradual relaxation of stresses along the duct walls are associated with the decreasing order of the birefringence bands along the length of the duct from its entrance [41]. Piau et al. (1995) made measurements in fluorinated and untreated dies to investigate the influence on the wall slip velocity of a polybutadiene. They used flow visualisation techniques for stress determination (by means of flow birefringence) and velocity measurements with a Doppler velocimeter. The LDV results indicated that no slip was detected near the wall for the flow in the steel die. For the fluorinated (PTFE) die, the level of stress applied to the polymer for a given flow rate decreased at the wall and outlet area, and surface cracks of extrudate were eliminated [42].

A number of theories and concepts for slip have been developed, resulting in a variety of molecular mechanistic and empirical models (see for example [26,43–47]). Different constitutive equations and slip models have been implemented in the computations of viscoelastic flows, examples include the finite element [2,48,49] and boundary element methods [50]. Several theoretical studies have reported that a slip boundary condition can enhance the stability in numerical calculations, reduce the amount of extrudate swell and alleviate the apparent stress singularity at die exits [48–50]. In addition, a multi-mode slip velocity model has been developed to describe experimental results quantitatively [44]. Hence, a spectrum of relaxation times (in both integral and differential type constitutive equation) is recommended. Of particular relevance to this paper is the work by Wang et al. [18], as they discuss a limiting stress for a polymer, above which slip will occur.

In this paper, we match experimentally obtained pressure difference and flow birefringence with the predictions of numerical simulations. The experimental data for a commercial LLDPE is obtained from a recently developed multi-pass rheometer (MPR) [51,52]. This machine is capable of generating precise, repeatable results under accurately controlled flow conditions and, consequently, we are confident in the data. A standard protocol for establishing rheological data was used and we are reasonably certain that our data reflect the correct rheology of the material under test. This data is used in a commercial simulation package, POLYFLOW [53], to predict the MPR experimental conditions. For the material used, we believe that POLYFLOW is producing a realistic simulation of the flow behaviour. In general, a zero wall slip boundary condition is applied to the flow situation, however, in cases where there is a clear discrepancy between experiment and simulation, we have introduced different levels of slip in the simulations. Thus, we have been able to identify the relative importance of slip for different processing conditions. The effect of viscous heating was also considered. The experimental techniques are described in Section 2, followed by the numerical approach, then both experimental data and simulations are compared for different flow situations, and we conclude with discussions.

2. Experimental

2.1. Material

The conventional Ziegler-Natta based LLDPE (z-nLLDPE) used is a commercial product of Dow Chemicals (Dowlex^{TM} NG5056E). A previous study has concluded that this material can be regarded as an *immiscible* blend of linear high molecular mass component and short-chain branched molecules of lower molecular mass [54], which is consistent with the information we received from the supplier [55]. Some material properties of the z-nLLDPE are listed in Table 1.

Table 1
Characteristics of the LLDPE investigated

Density (g cm^{-3})	0.919
M_w	113000
Polydispersity index	2.22
Melt index (190°C/2.16 kg), g/10 min	1.1
Zero shear viscosity (at 190°C)/Pa s	7.84×10^3

2.2. Characterisation

The rheology of the melt was modelled using the K-B.K.Z.-type integral constitutive equation with the Wagner irreversible single-exponential damping function [56], as given in Eq. (1)

$$\underline{\tau}(t) = -\int_{-\infty}^{t} \underbrace{\sum_{i=1}^{N} \frac{G_i}{\lambda_i} \exp\left(-\frac{t}{\lambda_i}\right)}_{\text{memory function}} \underbrace{\left\{\exp\left[-k\sqrt{\beta I_1 + (1-\beta) I_2 - 3}\right]\right\}}_{\text{Wagner damping function}} C^{-1}(t, t')\mathrm{d}t', \tag{1}$$

where $\underline{\tau}(t)$ is the total extra stress tensor; $C^{-1}(t, t')$, the Finger strain tensor that describes the change in shape of a small material element between present and past times t and t', respectively. In general, the kernel of this equation includes a time-dependent (linear) memory function expressed as a spectrum of relaxation times (G_i, λ_i) and a strain-dependent damping function expressed in terms of the first and second scalar invariants (I_1 and I_2) of $C^{-1}(t, t')$.

The z-nLLDPE melt was characterised in simple shear using a controlled strain Rheometrics Dynamic Spectrometer RDSII in the parallel plate configuration. Measurements include dynamic viscoelasticity, steady-state viscosity and step-strain stress-relaxation modulus. The material parameters of this model: a discrete spectrum of relaxation times (G_i, λ_i) (8-modes) and the Wagner damping constant, k, were determined from the oscillatory and step-strain experiments, respectively. Meanwhile, the extensional constitutive parameter, β, was arbitrarily chosen as unity in the axisymmetric modelling for reasons discussed in Section 4. β is irrelevant in a planar extension and simple shear where both I_1 and I_2 are equal. Details of the method involved in parameter determination and applicability of this model in predicting the behaviour of different materials can be found in [57]. The material parameters obtained for the z-nLLDPE at 170 and 190°C are given in Table 2.

Table 2
Material parameters of the LLDPE melt determined from RDSII measurements at 170 and 190°C

170°C	λ_i (s)	2.50×10^{-3}	5.88×10^{-3}	1.38×10^{-2}	3.26×10^{-2}	7.67×10^{-2}	1.81×10^{-1}	4.25×10^{-1}	1
	G_i (Pa)	1.75×10^5	1.46×10^5	2.80×10^4	5.61×10^4	1.22×10^4	1.29×10^4	1.53×10^3	2.31×10^3
	k	0.16±01							
190°C	λ_i (s)	2.50×10^{-3}	1.14×10^{-2}	5.16×10^{-2}	2.35×10^{-2}	1.07	4.84	22.0	100.0
	G_i (Pa)	1.45×10^5	9.90×10^4	3.77×10^4	7.48×10^3	1.41×10^3	1.52×10^2	18.6	0.16
	k	0.230±0.003							

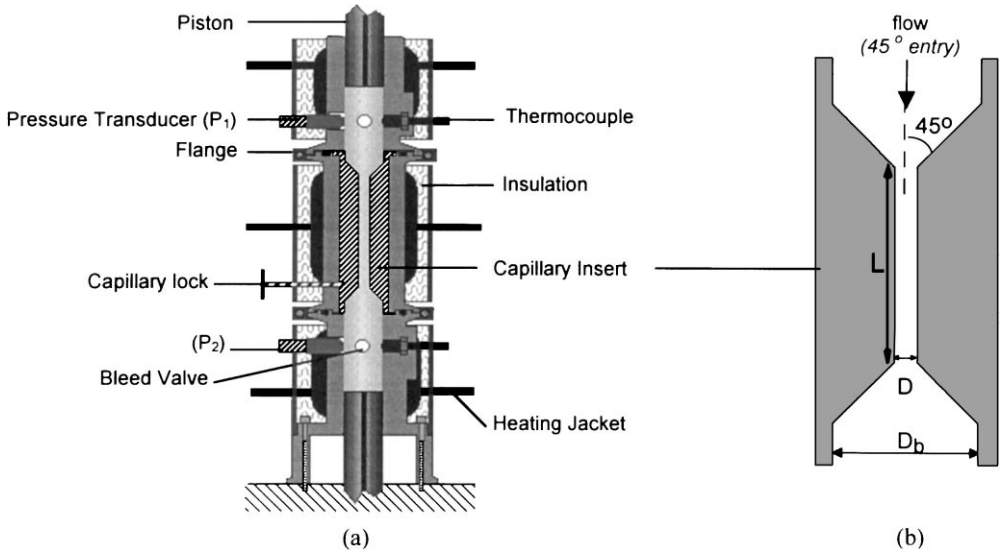

Fig. 1. (a) A schematic of a MPR with a capillary insert. The axial distance between the transducers (P_1 and P_2) is approximately 82 mm; the maximum piston stroke (centre-to-peak amplitude) in a multi-pass is 15 mm. (b) A schematic of the capillary insert (D_b=12 mm and dimension of the capillaries are given in Table 3).

2.3. Processing: the multi-pass rheometer

The multi-pass rheometer (MPR) has been under development in Cambridge for the last 5 years. This advanced form of capillary rheometer is capable of accessing processing performance, including the facility to perform flow birefringence observations. Recently, a study related to the processing behaviour of concentrated cellulose acetate solutions has illustrated how the MPR can be used in conjunction with rheological characterisation and numerical simulation [58]. The MPR has also been used for time-dependent capillary flow measurements of a HDPE melt [59].

A MPR with a capillary test section is shown schematically in Fig. 1(a). In general, the middle test section can be either a capillary holder or an optical cell (Fig. 3(a)). The entire system is controlled by a microcomputer that executes programs written with LABVIEW software for monitoring and data acquisition. Data acquisition includes reading piston position, pressure and temperature traces from the transducers and thermocouples. The specifications and operation details of a MPR may be found in [51,52].

The two pistons can be driven in a 'multi-pass' mode. A typical profile of the pressure difference (ΔP) and piston displacement in the 'multi-pass' steady-mode is shown in Fig. 2. As illustrated, both pistons are displaced synchronously at constant velocity (A→B) and a rapid pressure difference (V→W) develops across the sample within the test section. A steady-state ΔP (W→X) is attained while the pistons are still moving. Pressure relaxation of the material (X→Y) occurs during each dwell time (B→C) and ΔP subsequently diminishes (Y→Z). The remaining profiles were obtained for the reverse motion of the pistons, hence 'multi-pass'. In this study, we have used two types of test section to perform experiments in the steady-mode operation, and these are described in the following sections.

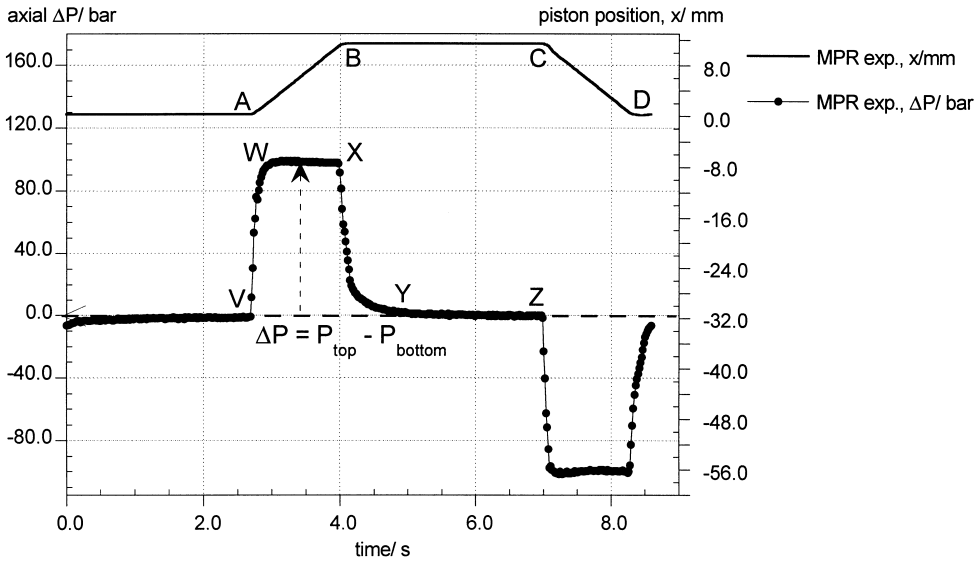

Fig. 2. 'Multi-pass' steady mode profile of the axial pressure difference and piston position as a function of time. Data of the z-nLLDPE at 190°C obtained using capillary 1 (L /D=40/4). Piston velocity, V_p=8.5 mm s^{-1}; centre-to-peak amplitude, a=5.5 mm; and idle time between successive passes, t=3 s.

2.3.1. Capillary flow

Experiments were carried out for the z-nLLDPE melt at 170 and 190°C using two different stainless-steel capillaries. A schematic of the capillary insert is shown in Fig. 1(b) and the dimensions are given in Table 3. The operating variables are piston velocity, idle time, amplitude of piston displacement, mean pressure and temperature. The settings are specified within the *Labview* program, except for temperature, which is controlled by the hot oil circulator. *Dynisco* pressure transducers of maximum range 350 bar were used to acquire pressure data. Measurements were taken with piston velocities ranging between 0.5 and 20.0 mm s^{-1}. The aim was to obtain the differential pressure across the capillary (ΔP) as a function of the imposed flow rate. The results obtained using both capillaries are given in Section 4.1.

2.3.2. Slit flow visualisation

An optical cell (Fig. 3(a)) was designed to fit rectangular die inserts of different slit geometry for the flow visualisation experiments. A schematic of the slit is shown in Fig. 3(b) and the dimensions are listed

Table 3
Dimensions of the capillaries and slit die used for experimentation with the LLDPE melt

Geometry of test section	Test temperature (°C)
Capillary 1 (extreme reduction ratio)[a]: L=40.0 mm, D=4.0 mm	190
Capillary 2 (mild reduction ratio)[a]: L=10.0 mm, D=8.0 mm	190
Slit die[b]: L=12.0 mm, w=1.0 mm, d=10.0 mm	170

[a] Entry/exit angle=45°.
[b] (Flat) entry angle=90°.

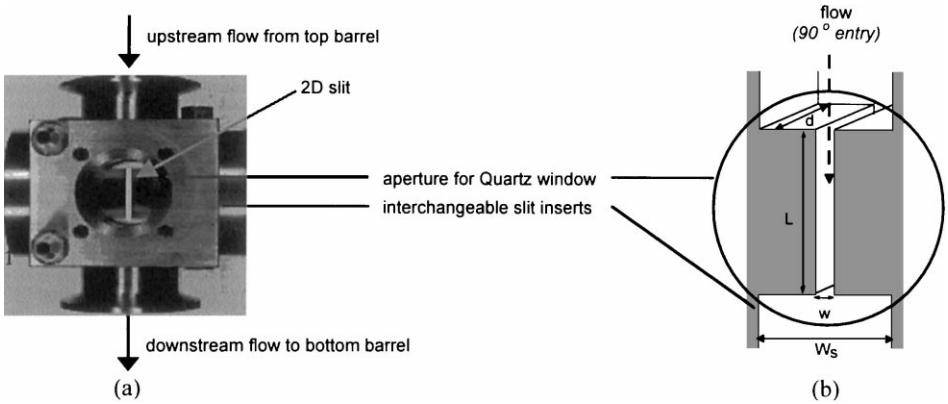

Fig. 3. (a) A stainless-steel optic cell. Shown are the 2D slit and slit inserts, a primary flow direction, and the aperture for the Quartz optic window of diameter 15.95 mm and length 15.0 mm. (b) A schematic of the 2D slit (width of the square cross-section, W_s=10.0 mm and dimension of the slit are given in Table 3).

in Table 3. Quartz optical windows of 15.95 mm diameter and 15.0 mm depth were manufactured with small angle bevels at the edges in order to reduce mechanical stress on the window.

The optical set up for flow-birefringence measurements is shown schematically in Fig. 4 and the main components are: a fibre optic light source; a filter and collimating lenses to generate a monochromatic parallel beam (of wavelength $\lambda=5.14\times10^{-7}$ m); and a polarizer and an analyzer oriented at mutually orthogonal positions on either side of the sample, with the polarizer inclined at an angle of 45° to the flow direction. A CCD camera detects the fringes transmitted through the analyzer. Image capturing and recording was performed by a workstation that consisted of a PowerMacintosh G3 with digital video-editing software, Adobe Premiere® 5.1 LE, and a Super VHS video set. The FIB pattern was analysed and processed using Adobe Photoshop® 5.0.2, image-editing software.

Flow-birefringence is an optical characteristic exhibited by molten polymer when it becomes anisotropic due to the effect of orientation during flow (see for example [60]). The level of anisotropy can be quantified according to the linear stress optical rule in terms of the principal stress difference (PSD), as given in

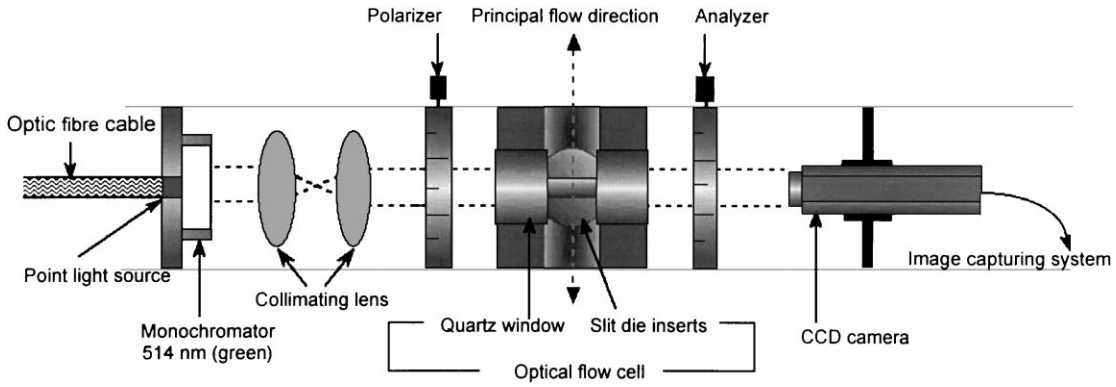

Fig. 4. A schematic of the flow visualisation set up in a MPR for capturing field-wise flow-birefringence.

Eq. (2). As such, the experimental PSD ($\Delta\sigma$) can be computed from the FIB patterns by counting the relative retardation (or fringe order), k, and assuming a typical value of the stress optical coefficient, C.

$$\Delta n = C(\Delta\sigma), \tag{2}$$

where Δn is the birefringence, which can be measured experimentally as Eq. (3)

$$\Delta n = \frac{k\lambda}{d}, \tag{3}$$

where λ is the wavelength of monochromatic light, and d the depth of sample through which the light propagates (see Fig. 3(b)).

3. The numerical approach

The MPR experiments were simulated using POLYFLOW, a commercial finite-element program primarily designed for the analysis of industrial flow processes dominated by non-linear viscous phenomena and viscoelastic effects [53]. In relation to simulation of polymeric fluids, POLYFLOW has been used in several experimental and/or theoretical studies of complex flows [2,48,58,61]. In general, the effects of gravity, inertia, compressibility, viscous heating and wall slip were neglected. However, in some cases we have incorporated either wall slip boundary conditions or viscous heating effect in the simulations. Two dimensional axisymmetric and planar simulations were carried out using rectangular element meshes that are similar to those used in the previous studies [2,58].

3.1. Viscoelastic isothermal flow and wall slip

The isothermal viscoelastic flow simulation involves solving the basic equations of mass and momentum conservation along with the K-B.K.Z. integral-type constitutive equation with the Wagner irreversible damping function and 8-mode relaxation time spectrum. The viscoelastic flow problem was solved within three stages and details of the numerical procedures used can be found in [2,62]. Numerical predictions of the steady-state axial pressure difference and centreline principal stress difference were compared with experimental observations. In cases where there is a discrepancy between the simulation and experiment, we introduced a slip boundary along the capillary or slit wall.

The wall slip boundary condition was modelled using a generalised *Navier* slip law with a power law tangential velocity dependence of the shear force, which can be expressed as

$$f_S = F_{slip}|v_S|^{exslip}, \tag{4}$$

where f_S is the *shear force*, v_S the *tangential velocity*, and the variables are *slip coefficient*, F_{slip} and *slip exponent*, exslip.

The velocity along the wall boundary can be obtained from the simulation results by considering a streamline closest to the wall. From the time integration of particle history along that streamline, the PSD and longitudinal component of the fluid velocity (v_y) can be obtained as a function of time (t). The axial displacement of material particle at time t_m is then calculated according to Eq. (5)

$$y = \int_{t_{en}}^{t} v_y \, dt \Rightarrow y_m = y_{m-1} + (t_m - t_{m-1})v_{y,m-1}, \tag{5}$$

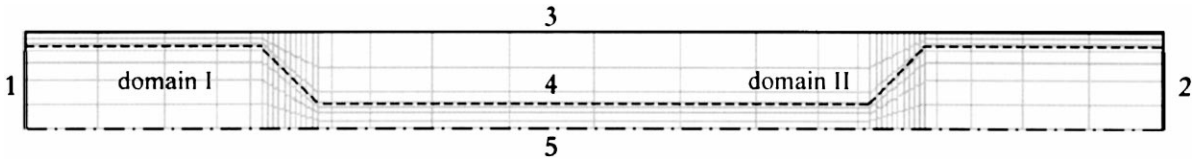

Fig. 5. Finite element mesh for the non-isothermal, generalised Newtonian and heat conduction flow simulation. The (watermark) mesh illustrates the flow boundaries (1: inflow; 2: outflow; 4: zero tangential velocity (no-slip); 5: axis of symmetry) and thermal boundaries (1: inlet flow temperature imposed; 3: insulated wall; 4: polymer/metal interface). Domain I (flow) and domain II (solid metal) are connected through the interface 4.

where $m \geq 1$ indicates subsequent discrete data points obtained from the particle tracking that begins at t_{en}, i.e. y_m at t_m is computed and the velocity v_y, can be obtained as a function of axial displacement, y.

3.2. Power law non-isothermal flow and viscous heating

The simulation of a non-isothermal flow involves solving the basic equations of mass, momentum and energy conservation along with the constitutive equation. The finite element mesh used (Fig. 5) consists of two domains with different subtasks. Domain I of this mesh is similar to the mesh used in Section 3.1. For the computation with viscous heating effect, we treated the problem (domain I) as a generalised Newtonian flow. The shear viscosity Eq. (6) is a power law function of the shear rate. Its temperature dependence follows the Arrhenius law

$$\text{Shear viscosity}: \ \eta(\dot{\gamma}, T) = \underbrace{m(\dot{\gamma})^{n-1}}_{\text{power law}} \exp\left[\alpha\left(\frac{1}{T} - \frac{1}{T_{\text{ref}}}\right)\right], \tag{6}$$

where $\alpha \equiv E_a/R$ is the activation energy ratio, T_{ref} the reference temperature, m and n the power law indices. The solid metal (domain II) is specified as a heat conduction task, where the thermal boundary conditions are as shown in Fig. 5. The effects of gravity, inertia, compressibility and wall slip were neglected.

4. Results

4.1. Capillary pressure difference data

Experimental and simulated pressure difference data are plotted as a function of mass flow rate in Figs. 6 and 7(a) and (b). Data for both capillaries are given in Fig. 6 for a processing temperature of 190°C. The experimental data shows a classic power law dependence and the numerical simulations match the experimental data very closely for both capillary geometries. The no-slip boundary condition used at the wall appears appropriate. All rheological parameters with the exception of the β parameter have been determined from separate experiments and, therefore, the good fit between simulation and experiment demonstrates that the constitutive equation and the no slip boundary conditions are appropriate for this process situation. Our simulations indicated that a higher value of β, can in general reduce the overall axial ΔP, i.e. it accelerates the damping function in extensional flow or decreases the extensional viscosity.

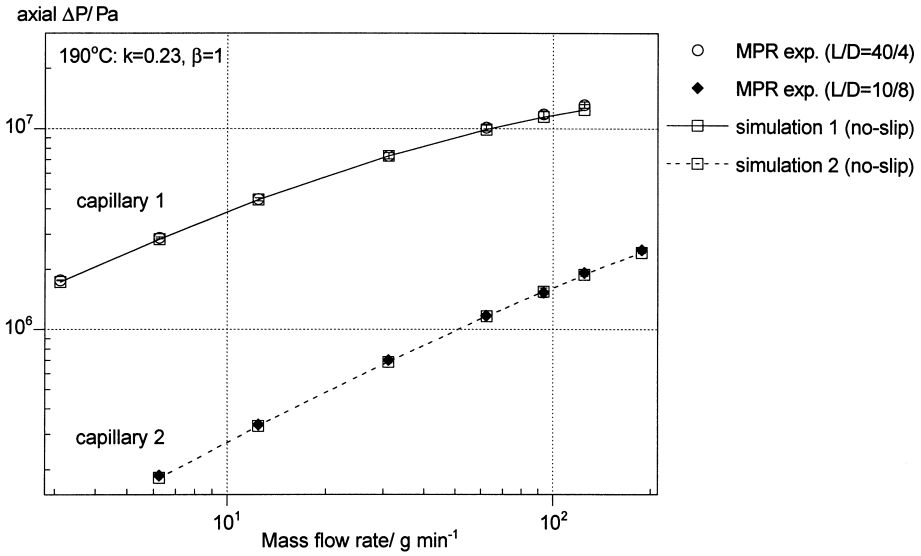

Fig. 6. Comparison between the measured and predicted axial pressure difference for steady-state axisymmetric capillary flow of the z-nLLDPE in capillary 1 and 2 at 190°C.

Nevertheless, this effect is only marginal and we have used a β value of unity in all simulations. In principle, the parameter β can be determined empirically from extensional flow data (see for example [3,62]).

Fig. 7(a) and (b) show the matching of simulation to experimental data for a processing temperature of 170°C. The lowering of the temperature has the effect of increasing pressure differences for the same mass flow rate, and we believe this has a significant effect. Fig. 7(a) shows the data and simulation for both capillaries and Fig. 7(b) the data and simulation for the longer capillary alone.

Fig. 7(a) shows that for the shallow capillary 2 the match between experiment and simulation is again good and the no-slip boundary condition holds. However, the higher pressure difference data shown in Fig. 7(a) for the longer capillary has a significant mismatch between experiment and simulated results. The experiment has been repeated on a number of occasions with different pre-shear thermal histories. On each occasion very similar data to that presented in Fig. 7(a), and in detail in Fig. 7(b), was obtained. If a no-slip boundary condition was used the simulation significantly overpredicts the experimentally observed pressure difference as shown in Fig. 7(b). If, however, a certain level of slip was introduced, a good match between simulation and experiment could be obtained, as shown in the figures. The amount of slip necessary to obtain a good match is discussed in Section 4.4.

4.2. Non-isothermal power law flow

In Section 4.1, we have shown that the discrepancy between the predictions and experimental data of capillary 1 at 170°C can be predicted by the presence of wall slip. Nevertheless, the effect of viscous heating could also be important. This was investigated numerically by using a power law approximation.

The simulations were carried out for non-isothermal power law flow in capillary 1 (domain I), which includes a solid metal (domain II) as shown in Fig. 5. For the polymer melt (domain I), the follow-

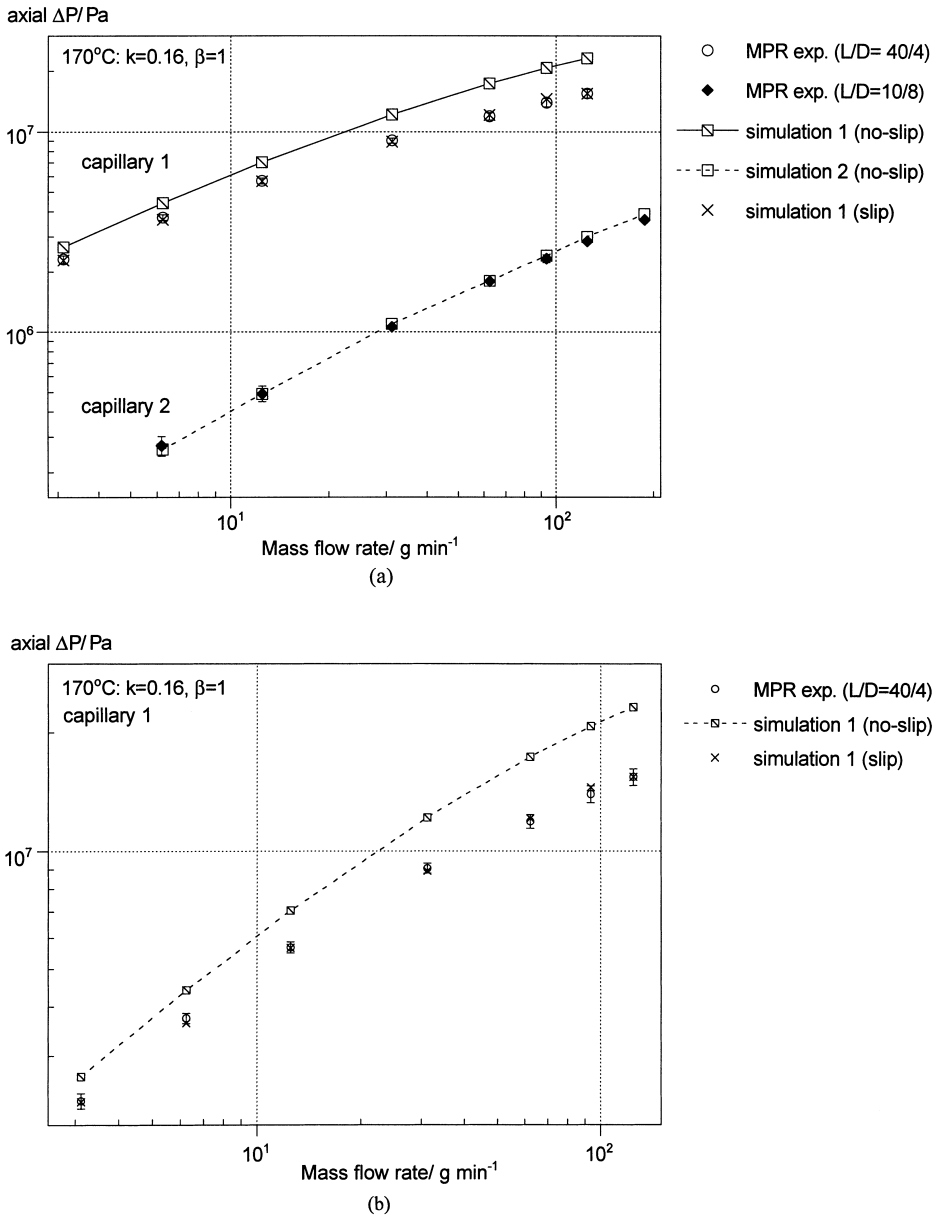

Fig. 7. Comparison between the measured and predicted axial pressure difference for steady-state axisymmetric capillary flow of the z-nLLDPE in: (a) capillary 1 and 2 at 170°C; (b) capillary 1 at 170°C. The simulation results shown are for *no-slip* (□) and slip (×) wall boundary conditions.

ing material data was specified: α=4053.404 K, T_{ref}=170°C; [power law 1 (m/Pa s$^{0.566}$)=1.85×10^4, n=0.566], [power law 2 (m/Pa s$^{0.59}$)=1.45×10^4, n=0.59]; thermal conductivity=0.5 W m^{-1} K^{-1}; specific heat capacity=2000 J kg^{-1} K^{-1} and density=919.5 kg m^{-3}. For the metal (domain II), the input was: thermal conductivity=35 W m^{-1} K^{-1} and initial temperature=170°C.

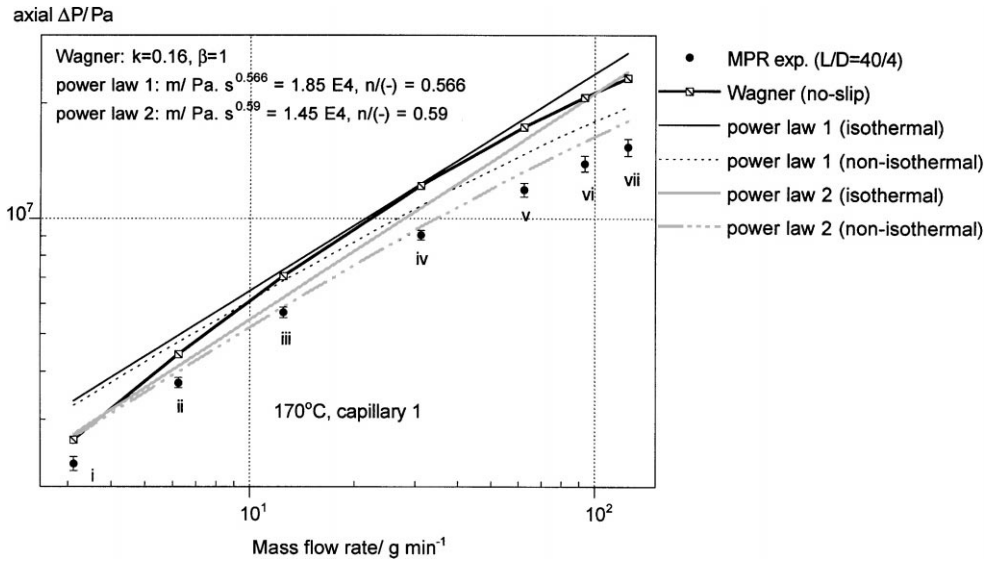

Fig. 8. Comparison between the measured and predicted axial pressure difference for steady-state axisymmetric capillary flow of the z-nLLDPE in capillary 1 at 170°C. The simulation results shown are for Wagner *no-slip*; power law *isothermal* (solid lines) and power law *non-isothermal* (dashed lines).

In Fig. 8, the MPR data at 170°C with capillary 1 and the Wagner simulations (*no-slip*) are plotted with the power law predictions for both isothermal and non-isothermal cases. In general, the power law model is applicable only for a certain range of the flow. As such, two sets of power law simulations have been carried out, each using different (*m*, *n*) indices, in order to mimic the Wagner (no-slip) flow curve. As can be observed in the figure, for the isothermal cases (solid curves) power law 1 and 2 are essentially the upper and lower bound of the Wagner (*no-slip*) flow curve. The predictions of power law 1 for the data points (iii, iv, v) and power law 2 (i, ii, vi, vii) appear comparable to the Wagner solutions (without imposed wall slip BC and viscous heating).

The next step was to repeat the power law simulations for *non-isothermal conditions*. The results are shown as dashed lines in Fig. 8. For both sets (1 and 2), the 'softening' effect from viscous heating increased with the flow rate. If we examine the power law 1 (*non-isothermal*) curve at (iii, iv, v), the simulations are 20–25% higher than the measurements. The power law 2 (*non-isothermal*) curve at (i, ii, vi, vii) are still 7–17% higher than the MPR data. At the high stress levels encountered in capillary 1, the simulation shows that some shear heating does appear to occur and the flow pressure is reduced. However, the magnitude of reduction is unable to account for the mismatch in our data and viscoelastic simulation.

4.3. Slit flow planar principal stress difference and pressure difference

Additional flow visualisation and pressure difference measurements were carried out in a slit geometry that enabled flow birefringence to be followed. Fig. 9 shows details of a particular flow birefringence pattern and Fig. 10 is a plot of the centerline |PSD| contour obtained from patterns of the type shown in Fig. 9. The stress field of the flowing polymer was mapped by the isochromatic bands that can be

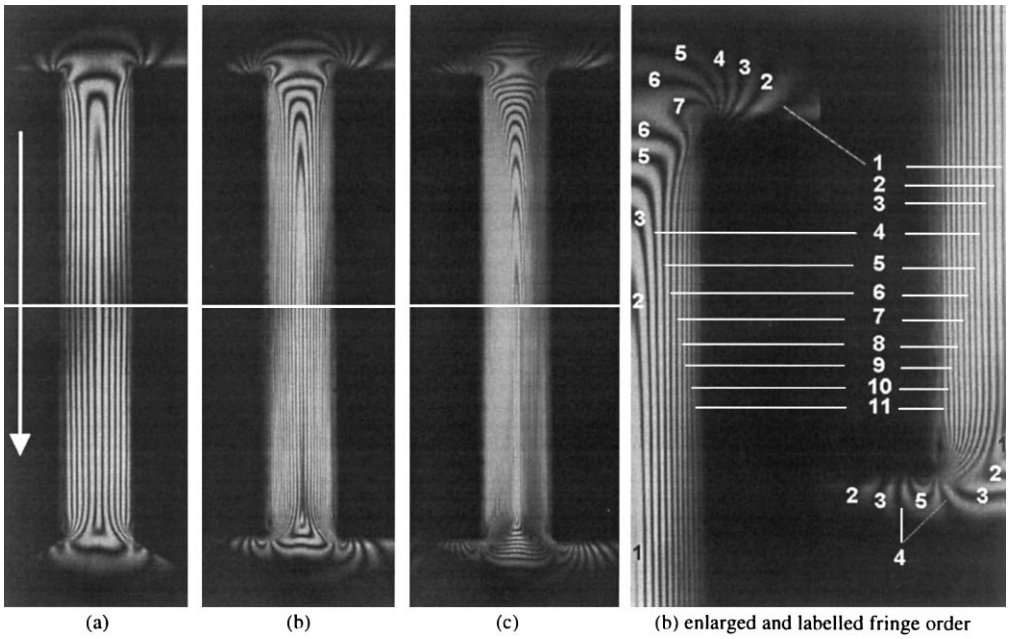

Fig. 9. Flow birefringence patterns of the z-nLLDPE for the flow into, within and exit from a slit (direction of primary flow is as shown by the arrow) at 170°C and mass flow rates (g min^{-1}) of: (a) 1.25, (b) 3.12, and (c) 9.36. Image (b) was enlarged to illustrate the level of retardation (indicated by the fringe order) and distribution of the isochromatics within the slit, in particular near the wall.

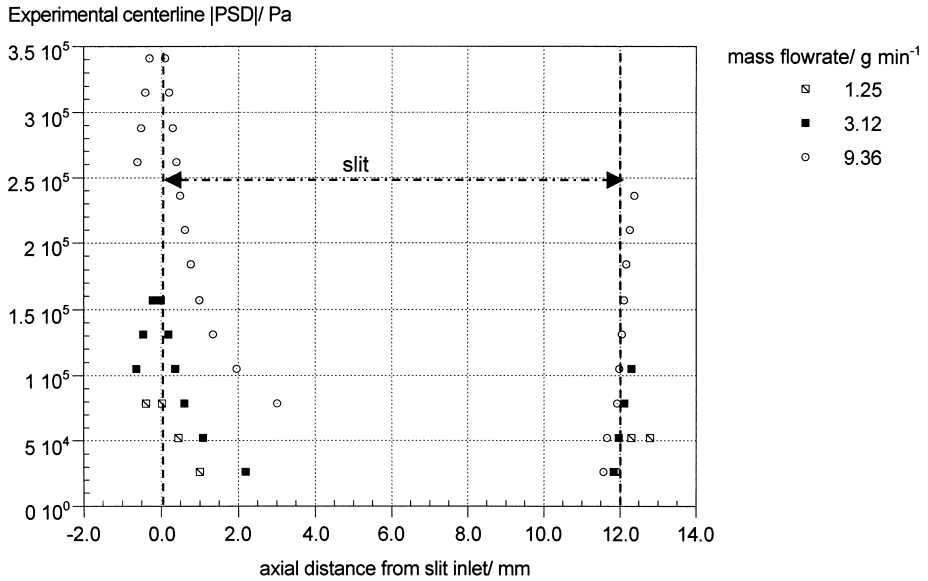

Fig. 10. Centerline |PSD| (as calculated from Eq. (2), stress optical coefficient C (Pa^{-1})=1.96×10^{-9}) as a function of position along centerline of slit for z-nLLDPE at 170°C and mass flow rates (g min^{-1}) of 1.25, 3.12, and 9.36.

quantified by counting the fringe order from start up (not shown here). The fringes emanate from the front corners of the slit entrance and develop from the two corners towards the centreline of the cell. As the pressure across the slit approaches steady state, this combined fringe splits in two and both parts move simultaneously in opposite directions, i.e. one part of the fringe moves into the slit section and the other moves into the upstream reservoir. Within the slit, the fringes tend to straighten out as they move further away from the slit entrance: parallel straight fringes represent a fully developed flow region. In principle, a central black fringe (zero order) should be observed in stress free regions, however, perhaps due to parasitic stress against the optical windows (see for example [60]), we have considered the lowest isochromatic band is of the first order.

The centreline principal stress difference of Fig. 9 was computed, assuming a reference value of the stress optical coefficient of 1.96×10^{-9} Pa^{-1} for LLDPE at 170°C. The *magnitude* of the principal stress difference, |PSD| as a function of axial distance from the slit inlet (y=0) for all the three flow rates are plotted in Fig. 10. As seen, the centreline |PSD| rises rapidly to a maximum value at the slit entrance, then decreases to a constant value at a distance of approximately 1–3 mm into the slit. At the exit, the |PSD| increases almost instantaneously, but did not reach a maximum value as observed for the entrance. Apart from the centreline, the |PSD| is a function of both shear stress and first normal stress difference, i.e. the |PSD| is defined as extensional stress along the centreline where the shear stress component is zero. Therefore, qualitatively the |PSD| reaches its maximum at the slit entry where material elements experience a maximum stretching; travelling away from the slit, material elements are not stretched, but are instead compressed, so a *decreasing* PSD is expected. However, the experimental technique used does not distinguish the sign of the PSD, so the results shown are only the magnitude.

The comparison of the experimental and predicted centreline |PSD| for a mass flow rate of 3.12 g min^{-1} as a function of axial distance is shown in Fig. 11. Despite the lack of visualisation further upstream

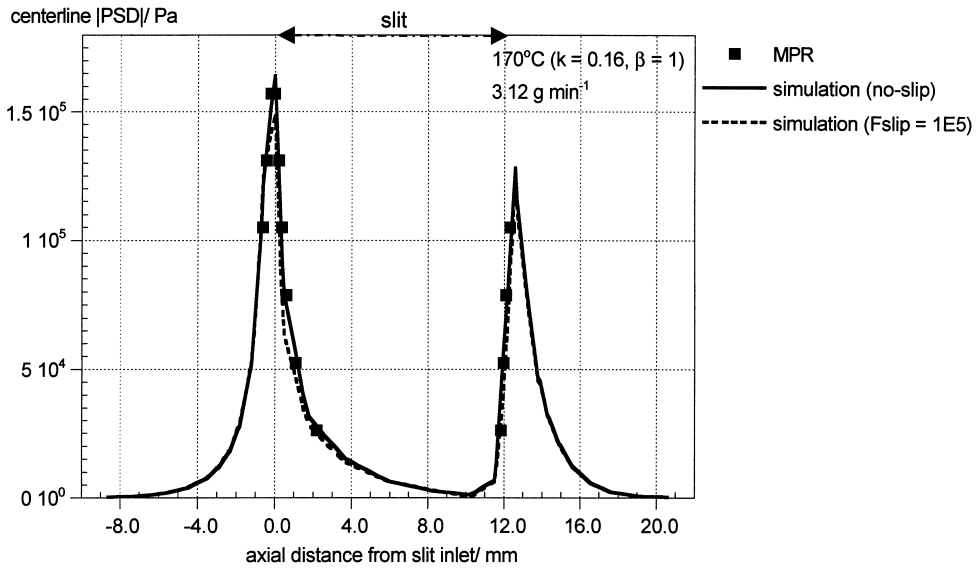

Fig. 11. Comparison of the experimental and predicted centerline |PSD|, as a function of position along centerline of slit for z-nLLDPE at 170°C and a mass flow rate of 3.12 g min^{-1}. The simulation results shown are for *no-slip* (solid line) and *slip* (dashed line) wall boundary condition.

Table 4
Experimental and predicted slit pressure difference, with and without slip in the simulations

Mass flow rate (g min^{-1})	Pressure difference (Pa)			Slip coefficient: F_{slip} (kg s^{-1})
	Experiment ($\Delta P_{Exp.}$)	Simulation ($\Delta P_{Sim.}$)	$\%\frac{\Delta P_{Sim.} - \Delta P_{Exp.}}{\Delta P_{Exp.}}$	Simulation
1.25	1.91×10^6	2.1×10^6	10.2	No-slip
3.12	3.50×10^6	4.0×10^6	16.1	No-slip
		3.9×10^6	12.1	5×10^5
		3.7×10^6	7.0	2×10^5
		3.4×10^6	−0.7	1×10^5
9.36	6.43×10^6	7.7×10^6	20.6	No-slip

and downstream of the slit, the stress field obtained is sufficient for meaningful comparison with the simulations. The simulated |PSD| with no-slip (solid line) and slip (dashed line) wall boundary conditions are both in reasonable agreement with the experimental observation and indicate that the wall slip introduction here does not have a significant effect on the centreline |PSD|.

The results of overall slit ΔP for all three flow rates are given in Table 4. In general, the predictions with no-slip BC are approximately 7–21% higher than the MPR data. For the case of mass flow rate 3.12 g mm^{-1}, a linear wall slip BC (exslip=0) was applied in order to predict correctly the overall axial ΔP. As the level of wall slip was increased, a good match was obtained using $F_{slip}=10^5$ kg s^{-1}, where the relative slip velocity was found to be 17.1% at the corresponding simulated wall shear stress of 0.13 MPa.

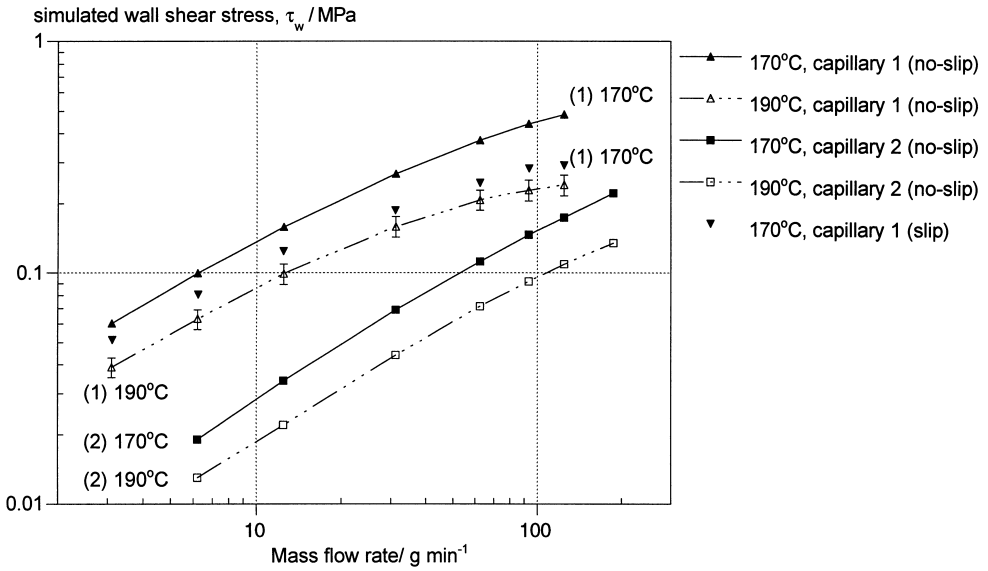

Fig. 12. Simulated wall shear stress within the slit for the z-nLLDPE as a function of mass flow rate.

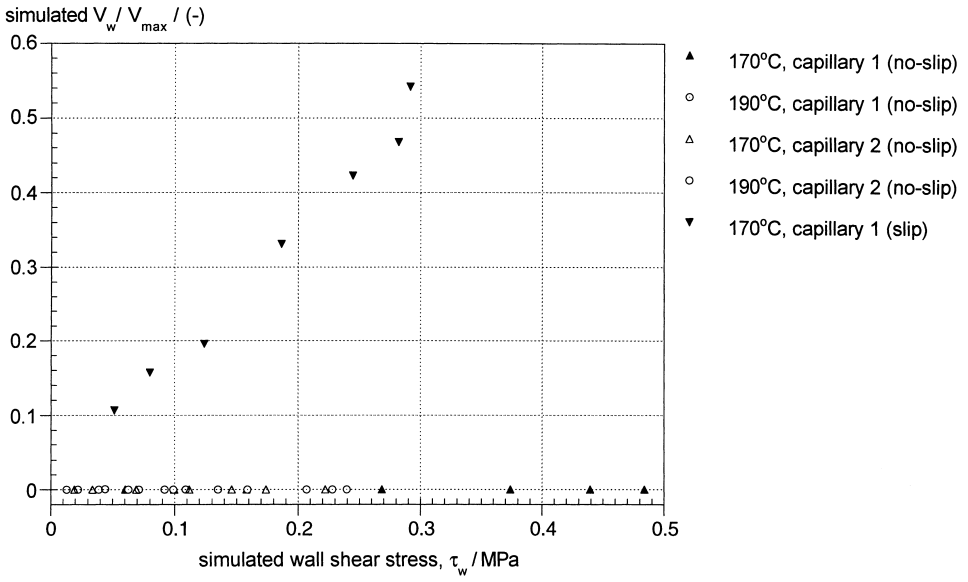

Fig. 13. Simulated ratio of wall to centerline velocity (V_w/V_{max}) within the slit as a function of the corresponding simulated wall shear stress for the z-nLLDPE.

4.4. Simulated flow curves and wall velocity: effect of slip/no-slip boundary conditions

The shear stress and longitudinal velocity as a function of axial position (Eq. (5)) were calculated for a streamline closest to the wall in the axisymmetric flow. Subsequently, average values of the wall shear stress and slip velocity were obtained for each of the flow rates. Fig. 12 is a plot of the simulated wall shear stress as a function of imposed flow rate for both temperatures. The data represent the actual flow conditions that have been simulated points (the lines are to facilitate the comparison between different set of results). In general, the relative order of the flow curves displayed a correct trend.

Fig. 12 shows the magnitude of the simulated wall stress as a function of mass flow rate for both capillaries at both temperatures. This plot shows that for the shallow capillary 2 the shear stress level is usually modest and a no-slip boundary condition appears effective. For capillary 1 the stress levels are generally higher and for the 170°C simulation the shear stresses without slip exceeded 0.3 MPa. In order to match the experimental data it was necessary to introduce slip, thereby limiting the maximum shear stress to of order 0.15 MPa.

The amount of slip necessary to match the high stress data is shown in Fig. 13, where the ratio of the wall simulated velocity to centreline velocity is plotted. From this plot, it can be seen that at the highest shear stress level a significant amount of wall slip is necessary to match the data.

5. Discussions and conclusions

We have shown in this paper that the MPR is capable of generating precise pressure difference and flow birefringence data; and that with the exception of our 170°C long capillary data the POLYFLOW

simulation using a K-B.K.Z. Wagner viscoelastic integral equation gives an impressive agreement between experiment and simulation.

The long capillary, 170°C data, however, clearly does not give a satisfactory match if a no-slip boundary condition is used in the isothermal simulations. We have decoupled the effect of slip and shear heating in the simulations, and used a power law approximation to simulate the non-isothermal flow. Our matching with the non-isothermal power law simulations suggest that high shear rate viscous heating could partly but not completely explain the overprediction of stress. Our viscoelastic slip simulations therefore represent an upper bound for the amount of slip necessary to match simulation to experiment.

The viscoelastic predictions of the wall shear stress plotted as a function of mass flow rate shown in Fig. 12 have striking similarities to that reported by Wang et al. [18], where they show that polymer melt appears to approach a limiting maximum shear stress. Our results appear to be consistent with this, and show that at a high shear stress, slip progressively appears to develop at the wall. This explanation is clearly tentative; therefore, we hope to substantiate the result in the future by direct-coupled PIV (particle imaging velocimetry) measurements at and near the wall.

The centreline flow birefringence experiments have also shown that the match between simulation and experiment is good; and in this particular case the presence of wall slip was found to have a negligible effect on the magnitude of the simulated |PSD|. Thus, in order to be confident that the simulation is performing well for the whole flow, it is important to ensure that both the overall pressure difference and the centreline |PSD| are consistent with experimental observations.

Acknowledgements

Financial support from the Commission of European Union through the BRITE-EURAM III ART project (BE96-3490) is gratefully acknowledged. We would also like to thank Dow Chemicals and Dr. R.J. Koopmans for their interest in this work.

References

[1] F.P.T. Baaijens, Mixed finite element methods for viscoelastic flow analysis: a review, J. Non-Newtonian Fluid Mech. 79 (1998) 361–385.
[2] R. Ahmed, R.F. Liang, M.R. Mackley, The experimental observation and numerical prediction of planar entry flow and die swell for molten polyethylene, J. Non-Newtonian Fluid Mech. 59 (1995) 129–153.
[3] D.G. Kiriakidis, H.J. Park, E. Mitsoulis, B. Vergnes, J.-F. Agassant, A study of stress distribution in contraction flows of an LLDPB melt, J. Non-Newtonian Fluid Mech. 47 (1993) 339–356.
[4] J.F.M. Schoonen, Determination of rheological constitutive equations using complex flows, Ph.D. thesis, Eindhoven University of Technology, The Netherlands, 1998.
[5] A.A. Collyer, D.W. Clegg, Rheological Measurement, 2nd Edition, Chapman & Hall, London, UK, 1998.
[6] R.G. Larson, A critical comparison of constitutive equations for polymer melts, J. Non-Newtonian Fluid Mech. 23 (1987) 249–269.
[7] R.G. Larson, Constitutive equations for polymer melts and solutions, Butterworths, Boston, 1988.
[8] E.B. Bagley, I.M. Cabott, D.C. West, Discontinuity in the flow curve of polyethylene, J. Appl. Phys. 29 (1) (1958) 109.
[9] J.J. Benbow, P. Lamb, New aspects of melt fracture, SPE Trans. 3 (7) (1963) 7–17.
[10] J.M. Dealy, Flow instabilities as stress limiters for molten polymers, in: C. Gallegos, A. Guerrero, J. Muñoz, M. Berjano (Eds.), Proceedings of the Fifth European Rheology Conference on Progress and Trends in Rheology, Portoroz, Slovenia, Springer, Berlin, 1998.

[11] M.M. Denn, Issues in viscoelastic fluid mechanics, Annu. Rev. Fluid Mech. 22 (1990) 13–34.
[12] P. Debye, R.L. Cleland, Flow of liquid hydrocarbon in porous vycor, J. Appl. Phys. 30 (6) (1959) 843–849.
[13] M.M. Denn, Surface-induced effects polymer melt flow, in: P. Moldenaers, R. Keunings (Eds.), Proceedings of the XIth International Congress on Rheology on Theoretical and Applied Rheology, Brussels, Amsterdam, Elsevier, New York, Vol. 1, 1992.
[14] W.B. Black, M.D. Graham, Wall-slip and polymer-melt flow instability, Phys. Rev. Lett. 77 (5) (1996) 956–959.
[15] R.G. Larson, Slip of polymer melts and solutions, in: A. Aït-Kadi, J.M. Dealy, D.F. James, M.C. Williams (Eds.), Proceedings of the XIIth International Congress on Rheology, Quebec City, Quebec, 1996.
[16] R.G. Larson, Instabilities in viscoelastic flows, Rheol. Acta 31 (1992) 213–263.
[17] C.J.S. Petrie, M.M. Denn, Instabilities in polymer processing (Journal Review), AIChE J. 22 (2) (1976) 209–236.
[18] X. Yang, H. Ishida, S.-Q. Wang, Wall slip and absence of interfacial flow instabilities in capillary flow of various polymer melts, J. Rheol. 42 (1) (1998) 63–80.
[19] D.S. Kalika, M.M. Denn, Wall slip and extrudate distortion in linear low-density polyethylene, J. Rheol. 31 (8) (1987) 815–834.
[20] J.P. Tordella, Unstable flow of molten polymers: a second site of melt fracture, J. Appl. Polym. Sci. 7 (1963) 215–229.
[21] A. Rudin, H.P. Schreiber, D. Duchesne, Use of fluorocarbon elastomers as processing additives for polyolefins, Polym.-Plast. Technol. Eng. 29 (3) (1990) 199–234.
[22] J.M. Piau, N. El Kissi, F. Toussaint, A. Mezghani, Distortions of polymer melt extrudates and their elimination using slippery surfaces, Rheol. Acta 34 (1995) 40–57.
[23] S.G. Hatzikiriakos, J.M. Dealy, The effect of interface conditions on wall slip and melt fracture of high density polyethylene, paper presented at ANTEC 91, SPE Tech. Papers 37, 1991, p. 2311.
[24] S.G. Hatzikiriakos, J.M. Dealy, Effects of interfacial conditions on wall slip and sharkskin melt fracture of HDPE, Int. Polym. Processing VIII 1 (1993) 36–43.
[25] S.G. Hatzikiriakos, P. Hong, W. Ho, C.W. Stewart, The effect of Teflon™ coatings in polyethylene capillary extrusion, J. Appl. Polym. Sci. 55 (1995) 595–603.
[26] R.S. Jeyaseelan, J.M. Dealy, A.D. Rey, Wall slip of molten polymers recent observations, in: A. Aït-Kadi, J.M. Dealy, D.F. James, M.C. Williams (Eds.), Proceedings of the XIIth International Congress on Rheology, Quebec City, Quebec, 1996.
[27] J.L. den Otter, J.L.S. Wales, J. Schijf, The velocity profiles of molten polymers during laminar flow, Rheol. Acta 6 (1967) 205–209.
[28] G.V. Vinogradov, L.I. Ivanova, Viscous properties of polymer melts and elastomers exemplified by ethylene-propylene copolymer, Rheol. Acta 6 (1967) 209–222.
[29] M. Mooney, Explicit formulas for slip and fluidity, J. Rheol. 2 (1931) 210–223.
[30] A.V. Ramamurthy, Wall slip in viscous fluids and influence of materials of construction, J. Rheol. 30 (1986) 337.
[31] S.G. Hatzikiriakos, J.M. Dealy, Wall slip of molten high density polyethylenes. I. Sliding plate rheometer studies, J. Rheol. 35 (1991) 497.
[32] S.G. Hatzikiriakos, J.M. Dealy, Wall slip of molten high density polyethylenes. II. Capillary rheometer studies, J. Rheol. 36 (4) (1992) 703–741.
[33] H.M. Laun, Wall slip of polymer melts from squeeze flow and capillary rheometer, in: Progress and Trends in Rheology, Proceedings of the Fifth European Rheology Conference, Portoroz, Slovenia, Springer, Berlin, 1998.
[34] K.B. Migler, H. Hervet, L. Leger, Slip transition of a polymer melt under shear stress, Phys. Rev. Lett. 70 (1993) 287–290.
[35] L.R. Schmidt, A special mold and tracer technique for studying shear and extensional flows in a mold cavity during injection molding, Polym. Eng. Sci. 14 (1974) 797–800.
[36] G. Mennig, Visuelle Untersuchungen zum Wandgleitverhalten hochpolymerer Schmelzen, Rheol. Acta 15 (3/4) (1976) 199–205.
[37] E. Wassner, M. Schmidt, H. Münstedt, Entry flow of a low-density-polyethylene melt into a slit die: an experimental study by laser-Doppler velocimetry, J. Rheol. 43 (6) (1999) 1339–1353.
[38] M.R. Mackley, I.P.T. Moore, Experimental velocity distribution measurements of high density polyethylene flowing into and within a slit, J. Non-Newtonian Fluid Mech. 21 (1986) 337–358.
[39] H. Münstedt, M. Schmidt, E. Wassner, Stick and slip phenomena during extrusion of polyethylene melts as investigated by a laser-Doppler velocimetry, J. Rheol. 44 (2) (2000) 413–427.
[40] G. Sornberger, J.C. Quantin, R. Fajolle, B. Vergnes, J.F. Agassant, Experimental study of the sharkskin defect in linear low density polyethylene, J. Non-Newtonian Fluid Mech. 23 (1987) 123–135.

[41] G.V. Vinogradov, N.I. Insarova, B.B. Boiko, E.K. Borisenkova, Critical regimes of shear in linear polymers, Polym. Eng. Sci. 12 (5) (1972) 323–334.
[42] J.M. Piau, N. El Kissi, A. Mezghani, Slip flow of polybutadiene through fluorinated slits, J. Non-Newtonian Fluid Mech. 59 (1995) 11–30.
[43] F. Brochard, P.G. de Gennes, Shear-dependent slippage at a polymer/solid interface, Langmuir 8 (1992) 3033–3037.
[44] I.B. Kazatchkov, S.G. Hatzikiriakos, Dynamic interfacial behaviour of linear polymers, in: A. Aït-Kadi, J.M. Dealy, D.F. James, M.C. Williams (Eds.), Proceedings of the XIIth International Congress on Rheology, Quebec City, Quebec, 1996.
[45] J.R.A. Pearson, C.J.S. Petrie, On the melt-flow instability of extruded polymers, in: Proceedings of the Fourth International Congress on Rheology, 3, 1965, pp. 265–282.
[46] J.R.A. Pearson, C.J.S. Petrie, On melt flow instability of extruded polymers, in: R.E. Wetton, R.H. Whorlow (Eds.), Polymer Systems: Deformation and Flow, Macmillan, London, 1968, pp. 163–187.
[47] J.M. Piau, N. El Kissi, Measurement and modelling of friction in polymer melts during macroscopic slip at the wall, Non-Newtonian Fluid Mech. 54 (1994) 121–142.
[48] P. Jay, J.M. Piau, N. El Kissi, J. Cizeron, The reduction of viscous extrusion stresses and extrudate swell computation using slippery exit surfaces, J. Non-Newtonian Fluid Mech. 79 (1998) 599–617.
[49] R.D. Wesson, T.C. Papanastasiou, Flow singularity and slip velocity in plane extrudate swell computations, J. Non-Newtonian Fluid Mech. 26 (1988) 277–295.
[50] N. Phan-Thien, Influence of wall slip on the extrudate swell: boundary element investigation, J. Non-Newtonian Fluid Mech. 26 (1988) 327–340.
[51] M.R. Mackley, P.H.J. Spitteler, Experimental observations on the pressure-dependent polymer melt rheology of linear low density polyethylene using a multi-pass rheometer, Rheol. Acta 35 (1996) 202–209.
[52] M.R. Mackley, R.T.J. Marshall, J.B.A.F. Smeulders, The multipass rheometer, J. Rheol. 39 (6) (1995) 1293–1309.
[53] M.J. Crochet, B. Debbaut, R. Keunings, J.M. Marchal, POLYFLOW: a multi-purpose finite element program for continuous polymer flows, in: K.T. O'Brien (Ed.), Applications of CAE in Extrusion and other Continuous Processes, Carl Hanser Verlag, Munich, Chapter 2, pp. 25–50, 1992.
[54] C. Gabriel, J. Kaschta, H. Munstedt, Influence of molecular structure on rheological properties of polyethylenes. I. Creep recovery measurements in shear, Rheol. Acta 37 (1998) 7–20.
[55] R.J. Koopmans, Dow Chemical Company, Terneuzen, Netherlands, private communication, 1998.
[56] M.H. Wagner, Rheol. Acta 18 (1979) 33.
[57] M.R. Mackley, R.T.J. Marshall, J.B.A.F. Smeulders, F.D. Zhao, The rheological characterisation of polymeric and colloidal fluids, Chem. Eng. Sci. 49 (1994) 2551–2565.
[58] W.-K. Wee, M.R. Mackley, The rheology and processing of a concentrated cellulose acetate solution, Chem. Eng. Sci. 53 (6) (1998) 1131–1144.
[59] M. Ranganathan, M.R. Mackley, P.H.J. Spitteler, The application of the multipass rheometer to time-dependent capillary flow measurements of a polyethylene melt, J. Rheol. 43 (2) (1999) 443–451.
[60] J.L.S. Wales, The application of flow birefringence to rheological studies of polymer melts, Ph.D. thesis, Technische Hogeschool Delft, The Netherlands, 1976.
[61] Y. Kanoh, T. Shibata, T. Nishimura, H. Usui, T. Saeki, in: A. Aït-Kadi, J.M. Dealy, D.F. James, M.C. Williams (Eds.), A Study on a Pipe Flow of Molten Polymer — An Investigation of Wall Slip by Visual Test and CAE, Proceedings of the XIIth International Congress on Rheology, Quebec City, Quebec, 1996.
[62] A. Goublomme, B. Draily, M.J. Crochet, Numerical prediction of extrudate swell of a high-density polyethylene, J. Non-Newtonian Fluid Mech. 44 (1992) 171–195.